

particles have substantially more of them. If these low coordination number corner and/or edge positions are implicated as active sites for toluene oxidation, then their relatively higher occurrence in the Au-Pd/C sample could account for the superior performance displayed by this catalyst. Another possible explanation could lie in the difference in the distribution of Au-Pd particle morphologies found in the two catalyst samples. The Au-Pd/C catalyst predominantly has multiply twinned (icosahedral and decahedral) particles, which tend to have {111} facet terminations. In comparison, the Au-Pd/TiO₂ materials show an increased fraction of cuboctahedral and singly/doubly twinned particles, which exhibit mixed {100}/{111} facet terminations. Hence, the increasing proportion of {100}-type facets in the Au-Pd/TiO₂ sample correlates with a lowering of the catalytic activity, and preparation strategies need to avoid them.

In a final set of experiments, we investigated the stability of the catalysts, because it is crucial to confirm that high-activity catalysts can be reused. With the Au-Pd/TiO₂ catalyst, the reaction was stopped after 7 hours, and the catalyst was recovered by decantation. Identical conversion was obtained on reuse of the Au-Pd/TiO₂ catalyst (Table 1, entries 14 and 15). For the Au-Pd/C catalyst, the reaction was stopped after 7 hours and the catalyst was allowed to settle. The liquid phase was then carefully removed by decantation

and fresh toluene was added. No metal was observed to have leached into the liquid phase during reaction, and the decanted liquid showed no further reaction in the absence of catalyst (fig. S7 and table S16). The reaction was then allowed to proceed for a further 7 hours, and the whole process was repeated a further two times. The reaction profile obtained with the decantation experiments was identical to that obtained with the fresh catalyst (fig. S8). Detailed STEM characterization shows that there is minimal particle growth or morphology change for the Au-Pd/C catalysts when studied over an extended reaction period (Fig. 1), during which catalysts were recovered after 31 and 65 hours of reaction, followed by two reuse cycles of 7 hours (figs. S9 and S10). Therefore, it is clear that any sintering or structural modification of these highly active catalysts is minimal, and we consider them to be stable and reusable.

References and Notes

1. R. A. Sheldon, J. K. Kochi, *Metal-Catalyzed Oxidations of Organic Compounds* (Academic Press, New York, 1981).
2. W. Partenheimer, *Catal. Today* **23**, 69 (1995).
3. Y. Ishii, S. Sakaguchi, T. Iwahama, *Adv. Synth. Catal.* **343**, 393 (2001).
4. K. Nomiya, K. Hashino, Y. Nemoto, M. Watanabe, *J. Mol. Catal. Chem.* **176**, 79 (2001).
5. T. G. Carrell, S. Cohen, G. C. Dismukes, *J. Mol. Catal. Chem.* **187**, 3 (2002).
6. S. Saravanamurugan, M. Palanichamy, V. Murugesan, *Appl. Catal. A Gen.* **273**, 143 (2004).

7. H. V. Borgaonkar, S. R. Raverkar, S. B. Chandalia, *Ind. Eng. Chem. Prod. Res. Dev.* **23**, 455 (1984).
8. M. L. Kantam *et al.*, *Catal. Lett.* **81**, 223 (2002).
9. Snia-Viscosa, *Hydrocarbon Proc.* **134**, 210 (1977).
10. F. Konietzki, U. Kolb, U. Dingerdissen, W. F. Maier, *J. Catal.* **176**, 527 (1998).
11. J. Zhu, A. Robertson, S. C. Tsang, *Chem. Commun. (Camb.)* **18**, 2044 (2002).
12. K. R. Seddon, A. Stark, *Green Chem.* **4**, 119 (2002).
13. X. Li *et al.*, *Catal. Lett.* **110**, 149 (2006).
14. F. Wang *et al.*, *Adv. Synth. Catal.* **347**, 1987 (2005).
15. J. Gao, X. Tong, X. Li, H. Miao, J. Xu, *J. Chem. Technol. Biotechnol.* **2002**, 620 (2007).
16. R. L. Brutchey, I. J. Drake, A. T. Bell, T. Tilley, *Chem. Commun. (Camb.)* **2005**, 3736 (2005).
17. A. P. Singh, T. Selvam, *J. Mol. Catal. Chem.* **113**, 489 (1996).
18. See supporting on Science Online for detailed methods.
19. J. K. Edwards *et al.*, *Science* **323**, 1037 (2009).
20. D. I. Enache *et al.*, *Science* **311**, 362 (2006).
21. J. Colby, D. I. Stirling, H. Dalton, *Biochem. J.* **165**, 395 (1977).
22. A. Wittstock, V. Zielasek, J. Biener, C. M. Friend, M. Bäumer, *Science* **327**, 319 (2010).
23. N. Dimitratos *et al.*, *Phys. Chem. Chem. Phys.* **11**, 5142 (2009).
24. A. Borodziński, M. Bonarowska, *Langmuir* **13**, 5613 (1997).
25. We acknowledge the support of the Dow Chemical Company through the Dow Methane Challenge.

Supporting Online Material

www.sciencemag.org/cgi/content/full/331/6014/195/DC1

Materials and Methods

Figs. S1 to S10

Tables S1 to S16

References

29 September 2010; accepted 14 December 2010

10.1126/science.1198458

Supracolloidal Reaction Kinetics of Janus Spheres

Qian Chen,¹ Jonathan K. Whitmer,^{1,2} Shan Jiang,¹ Sung Chul Bae,¹ Erik Luijten,^{3,4*} Steve Granick^{1,2,5*}

Clusters in the form of aggregates of a small number of elemental units display structural, thermodynamic, and dynamic properties different from those of bulk materials. We studied the kinetic pathways of self-assembly of “Janus spheres” with hemispherical hydrophobic attraction and found key differences from those characteristic of molecular amphiphiles. Experimental visualization combined with theory and molecular dynamics simulation shows that small, kinetically favored isomers fuse, before they equilibrate, into fibrillar triple helices with at most six nearest neighbors per particle. The time scales of colloidal rearrangement combined with the directional interactions resulting from Janus geometry make this a prototypical system to elucidate, on a mechanistic level and with single-particle kinetic resolution, how chemical anisotropy and reaction kinetics coordinate to generate highly ordered structures.

Clusters, an intermediate level of matter between building block (atom, molecule, or particle) and bulk phase, are found ubiquitously in nature and technology—for example, in the nucleation of bulk phases (1), nanoparticles (2), and protein aggregates in biology (3, 4). Whereas

structures that result from isotropic interactions between building blocks are well understood (5–8), it is more challenging to understand clusters formed from the common case of directional noncovalent interactions (9–17). On this question, we note that for molecular amphiphiles, such as surfactants, phospholipids, and many block copolymers, the segregation of their polar and nonpolar portions is a major mechanism steering the spontaneous formation of microstructured mesophases with fascinating and useful structures (9–11). Similarly, colloidal particles, larger than molecules but small enough to sustain Brownian motion, also assemble into clusters owing to directional noncovalent interactions (12–17). A largely unsolved problem is the question of commonality

between these fields. Therefore, combining amphiphilicity with colloidal rigidity, we study “Janus spheres” that are hydrophobic on one hemisphere and negatively charged on the other. An earlier publication from this laboratory described some structures that these hybrid materials form (18). Here, we address the kinetics of self-assembly at the single-particle level, showing that small, kinetically favored isomers join to form highly ordered but nonequilibrium large-scale structures.

A critical design rule is that the range of interparticle interactions (hydrophobic attraction and electrostatic repulsion) must be short relative to particle size and that the interactions must be reversible. Clustering then favors densely packed structures with at most six nearest neighbors per particle, in contrast to the more open and less ordered structures formed by particles whose interaction range is larger (13). At very low salt concentrations, particles repel one another electrostatically, whereas at high salt concentrations, van der Waals forces cause the particles to aggregate irreversibly (19). Therefore, we consider intermediate concentrations of monovalent salt at which amphiphilic clusters self-assemble (20).

If the hydrophobic patch is too small, assembly admits clusters composed of at most four particles. However, increase in patch size allows such clusters to grow into larger assemblies, with two constraints: First, particles must approach closely enough to experience hydrophobic attrac-

¹Department of Materials Science and Engineering, University of Illinois, Urbana, IL 61801, USA. ²Department of Physics, University of Illinois, Urbana, IL 61801, USA. ³Department of Materials Science and Engineering, Northwestern University, Evanston, IL 60208, USA. ⁴Department of Engineering Sciences and Applied Mathematics, Northwestern University, Evanston, IL 60208, USA. ⁵Department of Chemistry, University of Illinois, Urbana, IL 61801, USA.

*To whom correspondence should be addressed. E-mail: luijten@northwestern.edu (E.L.); sgranick@illinois.edu (S.G.)

tion; second, the number of nearest neighbors must not exceed six. For Janus particles whose hydrophobic domains are hemispheres, Fig. 1A displays pathways of reversible self-assembly, all of which we observed. They form a complex network in which multiple cluster possibilities emanate from every point and, likewise, routes from every point can meet. The hydrophobic patches lend appreciable orientational freedom to individual particles within the clusters. This promotes dynamical interconversion between clusters through three major mechanisms: step-by-step addition of individual particles, fusion of smaller clusters into a larger one, and isomerization. The clusters in this regime, with a size range $N = 2$ to 7 (fig. S1), are similar to those formed in depletion-induced assembly of homogeneous particles (5), except that for homogeneous particles the clusters must be kept isolated to avoid further aggregation. Here, cluster aggregation is prevented by electrostatic repulsion between the charged surface regions, allowing clusters to live in close proximity without fusing.

The ability to control the long-range repulsion makes it possible to switch on clustering at will by adding salt to Janus spheres in deionized water. We found that after the distribution of cluster sizes equilibrated (fig. S2), their shapes continued to change. For example, the capped trigonal bipyramid (CTBP) shape with cluster size $N = 6$ formed first, then gradually isomerized to the more symmetric octahedral shape (Fig. 1B). These kinetic data are consistent with a reversible first-order reaction with rate constants given in the figure caption. In this system, the octahedral shape is more stable. Nonetheless, the CTBP isomer forms first, because growth proceeds via rotation of a particle in a feeder cluster. Particles located at the cluster ends have the largest rotational freedom and thus act as the points where additional particles join the cluster, causing elongated structures to form. In a cluster, particles constantly jiggle about their mean positions; this process is analogous to highly excited vibrational motion in molecules, where the vibrations occasionally cause collective rearrangements. Molecular reaction dynamics occur on picosecond or faster time scales (21), whereas these colloidal transformations occur on the time scale of seconds and can be visualized one by one without ensemble averaging. These reaction dynamics are illustrated in movie S1, showing cluster growth from smaller clusters, and movies S2 and S3, showing cluster isomerization via different pathways. Unlike micelles formed from molecules, whose predominant growth mechanism is through addition of monomers to preexisting micelles (10), the rigid, spherical shape of these colloidal building blocks allows them to rotate without change of position such that clusters grow at their ends by fusing with other clusters. A second difference is that, unlike molecular micelles whose fluidity encourages shape to equilibrate rapidly, these colloidal clusters possess definite configurations. For the same number of particles in a cluster, there are distinctly different, long-lived shapes.

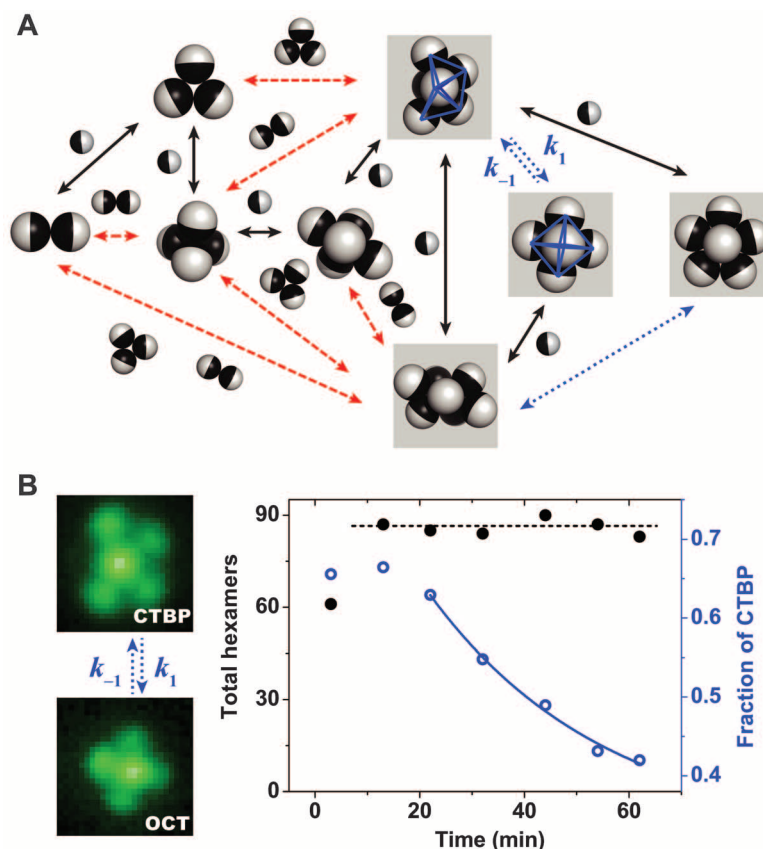


Fig. 1. Clusters formed from Janus spheres with one hydrophobic hemisphere. (A) Network of reaction pathways, all of which we have observed in experiments at 3.8 mM NaCl. Reaction mechanisms of monomer addition, cluster fusion, and isomerization are denoted by black, red, and blue arrows, respectively. Isomers with $N = 6$ and $N = 7$ elemental spheres are highlighted in boxes. Movie S1 shows a simple example of cluster growth by the fusion of two clusters. (B) A study of isomerization between two types of $N = 6$ clusters, the capped trigonal bipyramid (CTBP) and the octahedron (OCT). Here and in all other images, the Janus spheres have a diameter of 1 μm . After initiating the cluster process by setting the NaCl concentration at 3.8 mM, the partition of Janus spheres between clusters of different size equilibrates after 20 min (see fig. S2) but isomerization continues. Once the total number of hexamers (black filled circles) has stabilized, isomerization (fraction of CTBP, blue open circles) is consistent with first-order reaction kinetics in time t , $d[\text{OCT}]/dt = k_1[\text{CTBP}] - k_{-1}[\text{OCT}]$, time constant 34 min, $k_1/k_{-1} = 2.2$, and $k_1 = 0.02 \text{ min}^{-1}$. Here the calculation is based on the ensemble behavior of many clusters, among which individual ones can follow different reaction pathways. Movies S2 and S3 compare different pathways of isomerization.

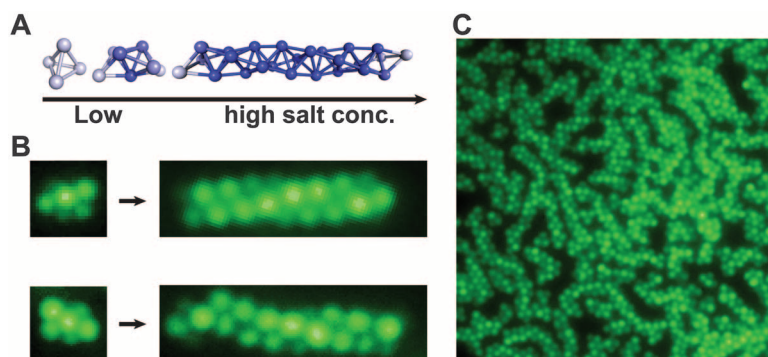


Fig. 2. Triple helices formed at higher salt concentration and higher particle concentration. (A) Geometrical representation of helix growth by face-sharing tetrahedra. (B) Comparison of a small chiral cluster (3.8 mM NaCl) and a longer helical cluster (5 mM NaCl). For both cases, fluorescence images of both right-handed and left-handed structures are shown. (C) Fluorescence image illustrating the stability of wormlike structures at high volume fraction. Movie S6 shows the fusion of two chiral chains by Brownian motion.

A minor increase of the salt concentration to 5 mM reduced the electrostatic repulsion to permit the growth of striking helical structures (Fig. 2). Closer inspection showed these to be Boerdijk-Coxeter (BC) helices (22), sometimes called Bernal spirals. The formation and stability of helices per se is a consequence of the directionality of the pairwise interactions, which allows them to persist up to the highest particle concentrations (60% after sedimentation), unlike homogeneous particles, which at lower particle concentrations form BC helices that become unstable when the concentration is higher (6, 7).

All dense packings of spheres on a cylindrical surface have the same internal energy, because each sphere except those at the ends of the chain interacts with six nearest neighbors (4). This remains true for Janus spheres, provided that each hydrophobic side faces the corresponding hemispheres of all neighbors—a constraint that is satisfied in the very structures that arise from the anisotropic interaction. This is analogous to carbon nanotubes, whose variety of rolled structures result from the same threefold coordinated graphene sheet (23). Thus, the absence of helical structures other than the BC helix indicates that either entropic or kinetic effects matter here.

To clarify the relative stability of a range of helical structures (4), we calculated their relative free energy as a function of Janus balance, taking into account the rotational entropy of individual Janus particles as well as vibrational modes; a related free-energy landscape is known for spheres

with isotropic interactions (5). As plotted in Fig. 3A, the 3(0,1,1) helix is in fact thermodynamically favored over the BC helix by a modest amount; here we use the notation proposed when this structure was identified (4). Strict quantitative correspondence to the experimental situation is not expected, as a full calculation including collective excitations and chain bending would be formidable to execute, but we can safely conclude that thermodynamically the BC helix is not strongly favored over the 3(0,1,1) helix (other tubular forms have a higher free energy).

Instead, we believe that the BC helices are the observed structure up to the highest particle concentrations because they are selected by kinetics. The preferred initial formation of CTBP $N = 6$ isomers, the basic building block of the BC helix, rather than octahedral $N = 6$ clusters, the basic unit of the 3(0,1,1) helix, causes the former helices to form first. Subsequent transformation relaxation of a BC helix into a 3(0,1,1) helix would require a massive collective change where, in the long-chain limit, one bond must be broken for every group of three spheres. This metastability explains why 3(0,1,1) helices are never observed in the experiment.

We confirmed the preferred formation of polytetrahedral over polyoctahedral clusters in molecular dynamics (MD) simulations, in particular at high attraction strengths where configurations tend to get trapped. Two further experimental observations strengthen this scenario. Although stable against relaxation into a 3(0,1,1) helix, the

BC helices occasionally display a spontaneous switch of handedness (movies S4 and S5). This is energetically slightly less costly, because only one bond needs to be broken for every four particles. More important, the possible pathway for chirality switching is simpler. Both chirality switching and relaxation to the 3(0,1,1) helix require unfavorable intermediate structures in which one particle has seven nearest neighbors. For the chirality switch, this pivotal particle has four bonds with reduced stability owing to large bond angles. If any of these bonds is broken, the chirality switching either proceeds or the chain returns to its original chirality. For the change from BC to 3(0,1,1), there are three bonds of reduced stability, and breaking any of these interrupts the transition; instead, it is one of the stable bonds that needs to be broken for the change to proceed, which is comparatively harder (fig. S3). Lastly, in both experiments (Fig. 3B) and MD simulations (Fig. 3C) we observe defects in which an $N = 7$ cluster is incorporated into a helix, reconfirming the kinetically arrested state of these structures, even though individual constituent spheres display considerable mobility. As expected for reversible self-assembly, these fibrillar clusters reform (heal) spontaneously after being torn apart by strong shear. They also fuse with one another through Brownian motion (movie S6) because the ends, which are most free to rotate, are more reactive than the middle.

Our results underscore the importance of kinetic selection when colloidal amphiphiles cluster. Unlike the rapid shape equilibration of molecular amphiphiles, Janus spheres present transient isomeric structures whose lifetime is so long that before isomers equilibrate they fuse to form the stable, highly ordered nonequilibrium helices described here. Their generalization to colloidal blocks of asymmetric shape (rods, ellipsoids, chains, etc.) presents an agenda for future work. This work on a prototypical system offers a direction in which to look for the design of new reconfigurable materials from the interplay between equilibration time scale and packing allowed by orientation-specific attraction.

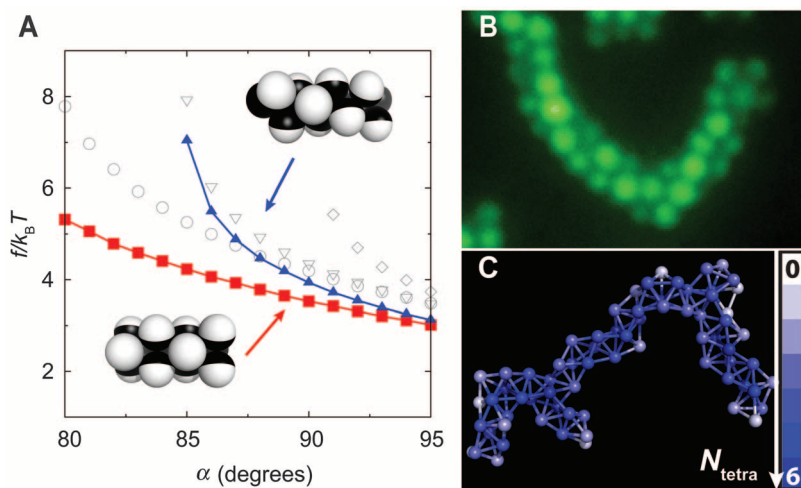


Fig. 3. Consideration of alternative tubular packings and defective structures. **(A)** Free energy per particle as a function of Janus balance α , half the opening angle of the hydrophobic patch. These tubular structures (4) are the 3(0,1,1) structure whose building block is the octahedral $N = 6$ isomer (red squares); the BC helix whose building block is the capped trigonal bipyramidal $N = 6$ isomer (blue triangles); also, for completeness, the 4(0,1,1) (circles), the (1,3,4) (inverted triangles), and the 2(1,1,2) (diamonds) structures, which have a higher free energy at the experimental Janus balance ($\alpha = 90^\circ$). Including vibrational entropy (5) reduces the free-energy difference between the 3(0,1,1) and the BC helix by $0.19 k_B T$ per particle for a representative chain length ($N = 24$). At $\alpha = 90^\circ$ this reduces the total free-energy difference by a factor of 2. The insets show schematic structures of the 3(0,1,1) and the BC helix. **(B)** Example of a kinked chain observed in experiments, in which an $N = 7$ cluster structure intercalates the predominant BC helix. **(C)** Similar structure, now with several intercalating $N = 7$ clusters, observed in molecular dynamics simulation. Particles are colored from white to blue depending on the number of tetrahedra in which they participate, N_{tetra} .

References and Notes

1. A. Cacciuto, S. Auer, D. Frenkel, *Nature* **428**, 404 (2004).
2. B. Yoon et al., *ChemPhysChem* **8**, 157 (2007).
3. T. P. Knowles et al., *Science* **318**, 1900 (2007).
4. R. O. Erickson, *Science* **181**, 705 (1973).
5. G. Meng, N. Arkus, M. P. Brenner, V. N. Manoharan, *Science* **327**, 560 (2010).
6. A. I. Campbell, V. J. Anderson, J. S. van Duijneveldt, P. Bartlett, *Phys. Rev. Lett.* **94**, 208301 (2005).
7. F. Sciortino, P. Tartaglia, E. Zaccarelli, *J. Phys. Chem. B* **109**, 21942 (2005).
8. J. Groenewold, W. K. Kegel, *J. Phys. Chem. B* **105**, 11702 (2001).
9. S. A. Safran, *Statistical Thermodynamics of Surfaces, Interfaces, and Membranes* (Addison-Wesley, Reading, MA, 1994).
10. I. A. Nyrkova, A. N. Semenov, *Macromol. Theory Simul.* **14**, 569 (2005).
11. S. Jain, F. S. Bates, *Science* **300**, 460 (2003).
12. S. C. Glotzer, M. J. Solomon, *Nat. Mater.* **6**, 557 (2007).
13. F. Sciortino, A. Giacometti, G. Pastore, *Phys. Rev. Lett.* **103**, 237801 (2009).

14. W. L. Miller, A. Cacciuto, *Phys. Rev. E* **80**, 021404 (2009).
15. S. Whitelam, S. A. F. Bon, *J. Chem. Phys.* **132**, 074901 (2010).
16. K. Liu et al., *Science* **329**, 197 (2010).
17. Z. Mao, H. Xu, D. Wang, *Adv. Funct. Mater.* **20**, 1053 (2010).
18. L. Hong, A. Cacciuto, E. Luijten, S. Granick, *Langmuir* **24**, 621 (2008).
19. J. W. Goodwin, *Colloids and Interfaces with Surfactants and Polymers* (Wiley, Chichester, UK, ed. 2, 2009), pp. 163–181.
20. See supporting material on Science Online.
21. J. Mikosch et al., *Science* **319**, 183 (2008).
22. A. H. Boerdijk, *Philips Res. Rep.* **7**, 303 (1952).
23. H. Dai, *Surf. Sci.* **500**, 218 (2002).
24. We thank J. Yan for discussions. Supported by the U.S. Department of Energy (S.G., Q.C., S.J.); Division of Materials Science, under award DE-FG02-07ER46471 through the Frederick Seitz Materials Research Laboratory at the University of Illinois at Urbana-Champaign (to S.G.); and by NSF grants CBET-

0853737 (S.C.B.) and DMR-0346914 and DMR-1006430 (J.K.W. and E.L., to E.L.).

Supporting Online Material

www.sciencemag.org/cgi/content/full/331/6014/199/DC1
Materials and Methods
Figs. S1 to S3
Movies S1 to S6
References

7 September 2010; accepted 9 December 2010
10.1126/science.1197451

The Deglacial Evolution of North Atlantic Deep Convection

David J. R. Thornalley,^{1,2*} Stephen Barker,¹ Wallace S. Broecker,³ Henry Elderfield,² I. Nick McCave²

Deepwater formation in the North Atlantic by open-ocean convection is an essential component of the overturning circulation of the Atlantic Ocean, which helps regulate global climate. We use water-column radiocarbon reconstructions to examine changes in northeast Atlantic convection since the Last Glacial Maximum. During cold intervals, we infer a reduction in open-ocean convection and an associated incursion of an extremely radiocarbon (^{14}C)–depleted water mass, interpreted to be Antarctic Intermediate Water. Comparing the timing of deep convection changes in the northeast and northwest Atlantic, we suggest that, despite a strong control on Greenland temperature by northeast Atlantic convection, reduced open-ocean convection in both the northwest and northeast Atlantic is necessary to account for contemporaneous perturbations in atmospheric circulation.

Vertical density gradients within the global ocean limit the exchange of surface and deep waters. Only in a limited number of locations, characterized by weak stratification of the water column and intense surface buoyancy losses, can surface water be converted into deep water by open-ocean convection (1). Through its

control on deepwater formation, open-ocean convection sets the properties of the deep global ocean and forms an essential component of the global overturning circulation (1).

Open-ocean deep convection in the North Atlantic occurs in the Labrador and Greenland Seas (1), transforming well-ventilated, nutrient-poor

surface waters into North Atlantic Deep Water (NADW), which spreads southward to occupy much of the deep Atlantic. Paleoceanographic studies suggest that deep convection in the North Atlantic was altered during the last ice age as compared with today [e.g., (2, 3)]. Glacial convection was shallower, forming Glacial North Atlantic Intermediate Water (GNAIW), and possibly weaker, leading to poorer ventilation of the deep Atlantic. Rapid fluctuations between weak and strong modes of deep convection could also be linked with abrupt climate changes across the North Atlantic region because of the associated changes in the poleward flux of warm surface waters. Furthermore, mode switches in deep convection might be triggered by changes in the input of fresh water, with the Younger Dryas (YD)

Fig. 1. (A) Surface and intermediate/deep ocean ^{14}C ventilation ages, with estimated uncertainty. Surface ocean estimates are from planktic foraminifera samples picked from the sediment cores: 12-1K, green line; 10-1P, blue line; 15-4P, red line; 17-5P, yellow line. Modern ventilation ages for the surface ocean and NADW are shown by the red and black arrow, respectively. Anomalous benthic ^{14}C dates are indicated by question marks. The date at 12 ka may contain reworked material because it is taken from within the Vedde Ash layer, the base of which consists of a basaltic turbidite. The anomalously young benthic ^{14}C date at 16.3 ka suggests contamination by modern carbon; we cannot, however reject this date with certainty, and it is possible that the young age is indicative of a brief interval of local convection, likely brine-induced. **(B)** Benthic-planktic foraminifera ^{14}C difference. Black arrow, modern surface-to-deep ^{14}C age difference. Dashed line in (A) and (B) indicates an interval of inferred local brine-induced convection. **(C)** Reconstructed surface seawater $\delta^{18}\text{O}$, corrected for global ice-volume changes, based on *N. pachyderma* (δ) $\text{Mg/Ca}-\delta^{18}\text{O}$ in 10-1P (22). **(D)** NGRIP $\delta^{18}\text{O}$ (11).

